Hysteresis-based mechanism for the directed motility of the Ncd motor

Sirish Kaushik Lakkaraju[1], Wonmuk Hwang[1,2*]

[1]Department of Biomedical Engineering, [2]Materials Science & Engineering Program,
Texas A&M University, College Station, Texas 77843, USA
[*]To whom correspondence should be addressed. Email:hwm@tamu.edu

Supporting Material

S1 Structure preparation and simulation protocol

We used PDB 1CZ7 (1), 1N6M (2), and 3L1C (3). While PDB 2NCD (4) also represents the pre-stroke conformation, we chose 1CZ7 as one of its chains has the neck coiled-coil visible by 7 more residues. There are point mutations in 1N6M (N600K) and 3L1C (T436S). We replaced them back to the wild-type (WT) residues. They are in the microtubule (MT) binding domain (N600) and the nucleotide-binding pocket (T436), and do not interact with the neck. The missing loops were filled using MODLOOP (5). None of these loops contact the neck except for L10 (E567–Q569). However, the L10-neck bonds (Fig. 1) broke during the motor head (MH) rearrangement phase of our restricted-perturbation targeted molecular dynamics (RP-TMD) simulation (6). Furthermore, alanine mutations in L10 had 99% of the MT gliding velocity of the WT (7), suggesting that L10 plays little role. The MH conformation is controlled by a biasing potential during RP-TMD simulations, and during equilibrium simulations the MT-binding domains were harmonically constrained, thus a bound nucleotide has no influence and was not modeled.

We applied harmonic constraints with a force constant of 5 kcal/(mol·Å^2) to all atoms of the protein except the added loops and the WT residues restored in the PDB structures (N600 for 1N6M and T436 for 3L1C), and the system was energy minimized by 400 steps of steepest descent followed by 1000 steps of adopted basis Newton-Raphson methods. The system was heated in an implicit solvent (Table S1) to 300 K with a rate of 5 K per 0.5 ps and equilibrated for 70 ps. During equilibration, velocities of atoms were rescaled if the simulation temperature deviated from 300 K by more than ±5 K. Subsequently, we applied harmonic constraints only to the protein backbone and further equilibrated the system for 200 ps. The integration time step used in this study was 1 fs. The equilibrated structures were used as the initial and target structures of the RP-TMD. For explicit-water RP-TMD simulations, our structures were prepared as follows: We built a solvation box of size 150 × 130 × 75 Å^3 around the pre- and post-stroke structures, and filled it with 45,973 water molecules. We then energy minimized and heated the system following the same protocol as mentioned above, with a periodic boundary condition applied to the simulation box. The structures were equilibrated for 500 ps with the backbone harmonically constrained with a force constant of 5 kcal/(mol·Å^2). These structures were used for explicit-water RP-TMD simulations.

For simulations of point mutations, side chains of the affected residues were replaced in the equilibrated structures as described above. The entire protein except for the mutated residues were harmonically constrained, and energy minimization and 100-ps equilibration MD at 300 K were performed to relax the mutated side chains. Similarly, in simulations where the neck has different conformations or sequences, the backbone of the replacing neck coiled-coil was aligned with that of the original one, followed by the energy minimization and equilibration procedure with harmonic constraints applied.

In RP-TMD, if the maximum allowed perturbation of the biasing potential (MAXF, in Å) is too small, the system does not reach the target structure. Conversely, too high values of MAXF leads to the system going over potential energy barriers that are otherwise inaccessible (6). In our system, we determined MAXF= 0.05 or 0.1 to be adequate. With these values, time to reach the target structure (root mean square deviation (RMSD) with the target less than 0.8 Å) was 18–92 ps (Table S1). The biasing potential of the RP-TMD was not applied to the loops constructed by MODLOOP. In RP-TMD trajectories, we considered a bond between residues to be formed when H and O atoms in respective side chains are closer than 2.4-Å. Coordinates were saved every 0.5 ps. In each coordinate frame, we calculated $R_{\rm tip}$ and made a list of MH-neck contacts. Across 10 simulations under each condition in Table S1, we built a histogram of bonds with a 2-Å bin size in $R_{\rm tip}$, which was used to calculate the probability as in Fig. 3.

S2 Explicit-water simulation of intermediate structures in RP-TMD

We took four intermediate structures in one of the 1CZ7 (pre)→1N6M (post) RP-TMD simulation with MAXF= 0.1 and in the ACE2 implicit solvent (Table S1). We also took another structure from the 3L1C (pre)→3L1C (post) RP-TMD simulation. These five structures represent: (a) Right before the breakage of R335-D424 bond ($R_{\rm tip} \sim 22$ Å, before **2** in Fig. 2), (b) After the breakage of R335-D424 and formation of the K336-D424 bond ($R_{\rm tip} \sim 35$ Å), (c) Formation of the K336-Q420 bond ($R_{\rm tip} \sim 60$ Å), (d) After **3** in Fig. 2, with the K336-E413 bond ($R_{\rm tip} \sim 80$ Å), and (e) From the RP-TMD of 3L1C, with the D344-K674 bond ($R_{\rm tip} \sim 7$ Å).

For each structure, we performed a 2-ns explicit water simulation with the backbone atoms in domains interfacing the MT ($L7$, $L11$ and $\alpha 4$) harmonically constrained with a force constant of 2.3 kcal/(mol·Å^2). The simulation followed the protocol mentioned above except that we used GROMACS (8) instead of CHARMM (9). Also, we neutralized the net charge of the system by randomly replacing 26 water molecules with Na^+ ions. The particle mesh Ewald summation method (10) was used to calculate electrostatic interactions. In cases (a)–(d), the intermediate bonds kept forming and breaking, with an average occupancy of 87% during the 2-ns simulation time. However, the N340-Y426 in (a) broke at 0.1 ns, and K674-D344 in (e) broke at 0.2 ns, and they stayed broken throughout the simulation.

S3 Choice of simulation modality for finding the transition path

In the original formulation of targeted molecular dynamics, transition between the initial and target structures is accomplished by applying a biasing force that reduces the RMSD between the two (11). Since the biasing force can push the system over large energy barrier that is otherwise inaccessible, in RP-TMD, the magnitude and direction of the biasing force is regulated so that the transition follows the minimum free energy path more closely (6, 12). In addition to RP-TMD, we initially considered the following two methods, which turned out to be unsuccessful.

In the normal mode superposition model (NMSM), normal modes of the two conformations of a protein are used to build a path between them (13). However, for Ncd, the cumulative involvement coefficient which measures the contribution of a given set of normal modes to the conformational transition, was only 0.49–0.51 for the first 100 modes, in contrast to 0.9 for myosin V between the rigor and post-rigor conformations (13). This implies that normal modes may not be directly related to the motion of Ncd's neck.

Minimum energy path (MEP) is a path optimization technique, where a trial path between two conformations (such as via linear interpolation) is refined using conjugate peak refinement (14).

While it was successfully used to find conformational changes across the relay helix that are coupled to the switch II during the recovery stroke of myosin (15), we could not determine the first order saddle points for the neck rotation in Ncd, possibly because the neck diffuses over a large range while forming multiple intermediate contacts. Without incorporating the effect of thermal fluctuation, MEP may not offer a good picture of such a transition (6, 16).

S4 Orientation of the neck

To measure the three angles defined in Fig. 1, we first assigned unit vectors along the axis of the neck; $\mathbf{u}_{\rm pre}$, $\mathbf{u}_{\rm post}$, and $\mathbf{u}$, respectively in the pre-, post-, and an intermediate state during the travel. If we denote the projection of $\mathbf{u}$ on the plane spanning $\mathbf{u}_{\rm pre}$ and $\mathbf{u}_{\rm post}$ by $\mathbf{u}'$, the angle between $\mathbf{u}_{\rm pre}$ and $\mathbf{u}'$ is $\theta_{\rm long}$, and that between $\mathbf{u}$ and $\mathbf{u}'$ is $\theta_{\rm trans}$. To measure $\theta_{\rm twist}$, we first translated the three conformations of the neck mentioned above so that their axes merge at the C-terminal end. The merging point of the three axes was used as a pivot for rotation. We rotated the intermediate structure (containing $\mathbf{u}$) towards $\mathbf{u}'$ by $-\theta_{\rm trans}$, followed by the rotation on the plane spanning $\mathbf{u}_{\rm pre}$ and $\mathbf{u}_{\rm post}$ by $-\theta_{\rm long}$. These operations align the neck in the intermediate state to the pre-stroke conformation without affecting rotation about its axis. For the neck each in the pre-stroke and intermediate conformations, we assigned local triads (17) (see the next section). $\theta_{\rm twist}$ is the axial rotation angle of the triads at the N-terminal end of the neck between the intermediate and pre-stroke conformations. In addition, rigid body rotation during the travel was quantified by measuring the axial rotation angles of the triads at the C-terminal end of the neck (close to the hinge). At the end of the travel, it was 10.5°. The net torsion in the neck is the difference between $\theta_{\rm twist}$ and the rigid-body rotation angle, which is $\simeq 21.8°$ for the trajectory used in Fig. 2.

S5 Deformation of the neck

Local Strain. We assigned local triads to individual α-helices and also to the neck coiled-coil as a whole. For the former, we assigned centroids of an α-helix with a 3-residue interval using C_α atoms in an overlapping manner (residue 297–299 for triad 1, 298–300 for triad 2, *etc*). In total there were 47 centroids on each α-helix. The arm $\mathbf{e}_3^{(n)}$ of the n-th triad ($n = 1 \cdots 46$) in the direction of the α-helical axis is defined along the line from the n-th to the $(n+1)$-th centroids. The second arm $\mathbf{e}_2^{(n)}$ is the unit vector normal to both $\mathbf{e}_3^{(n)}$ and a vector formed by connecting the n-th centroid to the second C_α among the three atoms defining the centroid. This fixes $\mathbf{e}_1^{(n)} = \mathbf{e}_3^{(n)} \times \mathbf{e}_2^{(n)}$.

The rotation angle between two successive triads about $\mathbf{e}_3^{(n)}$ represents the local twist, which can be found by calculating the corresponding Euler angle. Similarly, rotation angles about $\mathbf{e}_1^{(n)}$ and $\mathbf{e}_2^{(n)}$ quantify local bending in two orthogonal directions. The difference in the local twist angles between post- and pre-stroke structures provides the local torsional strain map shown in Fig. 4B.

Triads for the coiled-coil were defined similarly. We located the mid-point between each pair of centroids assigned to the two α-helices. The axial arm $\mathbf{e}_3^{(n)}$ of the triad is the unit vector along the line joining two successive mid-points. The next arm $\mathbf{e}_2^{(n)}$ is perpendicular to both $\mathbf{e}_3^{(n)}$ and the line joining the corresponding centroids of the individual α-helices, and $\mathbf{e}_1^{(n)} = \mathbf{e}_3^{(n)} \times \mathbf{e}_2^{(n)}$. Local strain was measured using the same method as for the individual α-helices. The difference in local torsional angles between the pre- and post-stroke structures of the neck is in Fig. S3A. The sum of local torsional angles lies in the 23.7°-27.2° range for the PDB structures tested, which is consistent with the net torsional angle calculated as a difference between $\theta_{\rm twist}$ and the rigid-body rotation angle in Sec. S4 above.

Torsional Energy. We isolated the neck (A295-R346) of PDB 1CZ7 and performed a 20-ns explicit-water MD simulation at 300 K. Denoting $\omega_i^{(n)}$ as the Euler angle divided by the length between triads n and $n+1$ of the coiled-coil with $\mathbf{e}_i^{(n)}$ as the rotation axis ($n = 1, \cdots, 46$), we measured its variance during the simulation, $\mathrm{var}(\omega_i^{(n)})$. The local stiffness $\kappa_i^{(n)}$ of the coiled-coil is (17)

$$\kappa_i^{(n)} = \frac{k_B T}{\mathrm{var}(\omega_i^{(n)})\Delta s} \tag{1}$$

where $\Delta s = 1.44$ Å is the average distance between triads. Using the torsional stiffness $\kappa_3^{(n)}$ and the measured local torsional angles of the traveling neck, we calculated the elastic energy in Fig. 4D.

S6 Tug-of-war sampling (TOWS)

For a given RP-TMD trajectory, we took structures with a spacing in R_{tip} by about 2 Å. For each structure, we harmonically constrained the MH backbone in the regions that are in the vicinity of the neck (I349-C352 (β1), D410-Y475 (α1-α2), E560-S575 (β6-β7), and L630-V645 (α5-β8)) with a spring constant of 5 kcal/(mol·Å^2), while fixing atoms in the rest of the MH that are further away. Instead of fixing, we also used harmonic constraints (spring constant 15 kcal/(mol·Å^2)) on the entire MH backbone, but the resulting potential of mean force (PMF) was similar (Fig. S4C). Since using harmonic constraints is computationally more expensive than fixing the MH atoms, for other TOWS simulations we used the latter.

For sampling, we applied another harmonic constraint on the S297 C_α atom at the N-terminal tip of the neck with a spring constant of 5 kcal/(mol·Å^2). Using 2 or 15 kcal/(mol·Å^2) did not affect the result (Fig. S4B). At each value of R_{tip}, we performed an 800-ps MD simulation at 300 K. Coordinates were saved every 1 ps. During the simulation, S297 C_α fluctuates around the center $\vec{r}_0$ of the harmonic potential. Denoting its deviation from $\vec{r}_0$ by $\vec{\delta}r$, the i-th ($i = 1, 2, 3$) Cartesian component of the force f_i on it at $\vec{r}_0$ is (18):

$$\begin{aligned} f_i &\simeq \frac{k_B T}{\mathrm{var}(\delta r_i)}\langle \delta r_i \rangle + \sum_{j \neq i} F_{ij}\langle \delta r_j \rangle, \\ F_{ij} &\simeq -k_B T \frac{\mathrm{cov}(\delta r_i, \delta r_j)}{\mathrm{var}(\delta r_i)\mathrm{var}(\delta r_j)}, \end{aligned} \tag{2}$$

where $\langle \cdot \rangle$ denotes average over the simulation time, var() and cov() are respectively variance and covariance, and F_{ij} is the second-order partial derivative of the free energy in the i- and j-directions. PMF was obtained by projecting the negative of force vectors (free energy gradient) along the path defining R_{tip} and integrating. For some structures we extended the simulation time up to 5 ns, but 800 ps was sufficient, which can also be seen by the nearly identical PMF profiles obtained from the first and second half of the 800-ps simulation (Fig. S4D). To further test the consistency of the PMF profile, we selected 11 intermediate structures from the explicit water RP-TMD simulation in the range R_{tip} = 16–40 Å over the first energy barrier (*cf.*, **2** in Fig. 5B) and performed TOWS simulation using the GBSW implicit solvent model (19). Consistent with PMFs obtained under other conditions, the energy barrier was preserved (Fig. S4A).

S7 First passage time

Treating the neck coiled-coil as a cylinder with diameter $d = 15.3$ Å and length $L = 75.4$ Å, its rotational diffusion coefficient D_r with one end (G347) pivoted is (20, 21)

$$D_r = \frac{3k_BT}{4\pi\eta L^3}[\ln(p) + \delta_r] \simeq 3.01 \times 10^6 \mathrm{rad}^2/s \tag{3}$$

where $p = L/d$ is the aspect ratio, $\delta_r = -0.662 + 0.917p^{-1} - 0.050p^{-2}$ is the correction factor accounting for the end effect, and $\eta = 8.56 \times 10^{-4}$ Ns/m^2 is the dynamic viscosity of water at 300 K.

If the neck does not interact with the MH and performs pure rotational diffusion with a pivoted end, the first passage time τ_{free} to reach $\theta_{\mathrm{long}} = 73.2°$ is

$$\tau_{\mathrm{free}} = \frac{\theta_{\mathrm{long}}^2}{2D_r} = 271 \text{ ns} \tag{4}$$

In the presence of the PMF $U(x)$ as in Fig. 5B, the first passage time from $x = 0$ to reach $x = R_{\mathrm{tip}}$ is (22)

$$\tau(R_{\mathrm{tip}}) = \frac{1}{L^2 D_r} \int_0^{R_{\mathrm{tip}}} dx\, e^{U(x)/k_BT} \int_0^x dy\, e^{-U(y)/k_BT}. \tag{5}$$

The first passage times for the two PMFs in Fig. S4A are plotted in Fig. S5.

In a 3-bead single molecule assay of Ncd (23), the moving part is a 4.3-μm long MT (25 nm in diameter), whose axial drag coefficient is $\zeta_{MT} = 4.67 \times 10^{-9}$ Ns/m (24). In addition, there are two 1-μm diameter beads attached to the ends of the MT, whose drag coefficient is $\zeta_b = 8.07 \times 10^{-9}$ Ns/m each. Compared to these, the drag coefficient of the moving MH that has a 20.3 Å radius of gyration is 3.28×10^{-11} Ns/m, which is negligible. The axial diffusion coefficient of the MT is then $D_{MT} = k_BT/(\zeta_{MT} + 2\zeta_b) = 1.99 \times 10^{-13}$ m^2/s. The first passage time can be estimated using Eq. 5, with D_{MT} replacing L^2D_r, which is $L^2D_r/D_{MT} = 857$ times longer than those for the case when the neck moves without load.

S8 RP-TMD simulation of mutants

N340K/K640N. A previous study showed that mutants N340K, K640N, or N340K/K640N have bidirectional motility with gliding velocities of axoneme-MT complexes comparable to that of the WT (25). We performed RP-TMD simulations of the N340K/K640N double mutant and calculated the PMF both for the forward and reverse travel. Swapping Asp and Lys between 340 and 640 resulted in loss of the bond between them in the forward travel and loss of the N340-R350 bond in both directions. Furthermore, the K336-Q420 bond did not form, indicating that point mutations can lead to changes in bond formation by other residues (Fig. 3D,K). PMFs for the N340K/K640N mutant are also different, rising nearly monotonically towards the post-stroke side without a clear barrier (Fig. S4E,F). The neck may thus simply fluctuate with the pre-stroke position as the bottom of the energy well. The loss in directionality in the neck motion may then allow bi-directionality in the MT gliding assay via a cooperative effect among multiple motors (25, 26).

N340A. The double mutant H339A/N340A had a moderate reduction in the MT gliding velocity, 79% of the WT value (7). Since the H339-S421 bond breaks quickly after the MH-rearrangement, loss in the N340-K640 bond (Figs. 2A and 3), may have a greater effect on motility. We thus performed RP-TMD simulations of the N340A mutant. In 8 out of 10 RP-TMD runs, the D344-K640 bond that overlaps with N340-K640 in WT (Figs. 2A and 3) remained intact, so that the

MH-neck contact involving K640 is maintained. This may be responsible for the moderate reduction in the MT gliding velocity.

Other mutants. We also performed RP-TMD simulations of eight other mutants including those with the neck replaced by the leucine-zipper or a random sequence (Ncd-ran12) (Table S1) (7). Overall, the contacts involving mutated residues were broken without affecting other bonds. In the case of leucine-zipper sequence, only N340 in the neck was conserved, which preserved the N340-K640 bond. However, with all other contacts lost, in a 1-ns regular MD simulation in the ACE2 implicit solvent, the neck detached from the pre-stroke position and swiveled. In Ncd-ran12, although all residues of the neck forming bonds with the MH are lost, alternative S336-D424 and K339-D424 bonds formed until $R_{\rm tip}$ ∼13.4–24.7 Å. However, these bonds were not enough to hold the neck in the pre-stroke position, and it also detached from the MH in a 1-ns MD.

References

[1] Kozielski, F., S. De Bonis, W. P. Burmeister, C. Cohen-Addad, and R. H. Wade. 1999. The crystal structure of the minus-end-directed microtubule motor protein ncd reveals variable dimer conformations. Structure. 7:1407–1416.

[2] Yun, M., C. E. Bronner, C. G. Park, S. S. Cha, H. W. Park, and S. A. Endow. 2003. Rotation of the stalk/neck and one head in a new crystal structure of the kinesin motor protein, Ncd. EMBO J. 22:5382–5389.

[3] Heuston, E., C. E. Bronner, F. J. Kull, and S. A. Endow. 2010. A kinesin motor in a force-producing conformation. BMC Struct. Biol. 10:19–31.

[4] Sablin, E. P., F. J. Kull, R. Cooke, R. D. Vale, and R. J. Fletterick. 1996. Crystal structure of the motor domain of the kinesin-related motor ncd. Nature. 380:555–559.

[5] Fiser, A., and A. Sali. 2003. ModLoop: automated modeling of loops in protein structures. Bioinformatics. 19:2500–2501.

[6] van der Vaart, A., and M. Karplus. 2005. Simulation of conformational transitions by the restricted perturbation–targeted molecular dynamics method. J. Chem. Phys. 122:114903.

[7] Sablin, E. P., R. B. Case, S. C. Dai, C. L. Hart, A. Ruby, R. D. Vale, and R. J. Fletterick. 1998. Direction determination in the minus-end-directed kinesin motor ncd. Nature. 395:813–816.

[8] van der Spoel, D., E. Lindahl, B. Hess, G. Groenhof, A. E. Mark, and H. J. C. Berendsen. 2005. GROMACS: Fast, flexible, and free. J. Comp. Chem. 26:1701–1718.

[9] Brooks, B., C. Brooks III, A. Mackerell Jr, L. Nilsson, R. Petrella, B. Roux, Y. Won, G. Archontis, C. Bartels, S. Boresch, et al. 2009. CHARMM: The biomolecular simulation program. J. Comp. Chem. 30:1545–1614.

[10] Darden, T., D. York, and L. Pedersen. 1993. Particle mesh Ewald: an N·log(N) method for computing Ewald sums. J. Chem. Phys. 98:10089–10092.

[11] Schlitter, J., M. Engels, P. Kruger, E. Jacoby, and A. Wollmer. 1993. Targeted molecular dynamics simulation of conformational change-application to the t↔r transition in insulin. Mol. Simulat. 10:291–308.

[12] van der Vaart, A., and M. Karplus. 2007. Minimum free energy pathways and free energy profiles for conformational transitions based on atomistic molecular dynamics simulations. J. Chem. Phys. 126:164106.

[13] Cecchini, M., A. Houdusse, and M. Karplus. 2008. Allosteric communication in myosin V: From small conformational changes to large directed movements. PLoS Comp. Bio. 4:e1000129.

[14] Fischer, S., and M. Karplus. 1992. Conjugate peak refinement: an algorithm for finding reaction paths and accurate transition states in systems with many degrees of freedom. Chem. Phys. Lett. 194:252–261.

[15] Fischer, S., B. Windshugel, D. Horak, K. C. Holmes, and J. C. Smith. 2005. Structural mechanism of the recovery stroke in the myosin molecular motor. Proc. Natl. Acad. Sci. USA. 102:6873–6878.

[16] Yu, H., L. Ma, Y. Yang, and Q. Cui. 2007. Mechanochemical coupling in the myosin motor domain. II. Analysis of critical residues. PLoS Comp. Biol. 3:e23.

[17] Lakkaraju, S. K., and W. Hwang. 2009. Modulation of elasticity in functionally distinct domains of the tropomyosin coiled-coil. Cell. Mol. Bioeng. 2:57–65.

[18] Hwang, W. 2007. Calculation of conformation-dependent biomolecular forces. J. Chem. Phys. 127:175104.

[19] Im, W., M. S. Lee, and C. L. Brooks. 2003. Generalized Born model with a simple smoothing function. J. Comp. Chem. 24:1691–1702.

[20] Broersma, S. 1960. Rotational diffusion constant of a cylindrical particle. J. Chem. Phys. 32:1626–1631.

[21] Tracy, M. A., and R. Pecora. 1992. Dynamics of rigid and semirigid rodlike polymers. Ann. Rev. Phys. Chem. 43:525–557.

[22] Gardiner, C. W. 2009. Stochastic methods: A Handbook for the Natural and Social Sciences, 4th Ed. Springer.

[23] deCastro, M., R. Fondecave, L. Clarke, C. Schmidt, and R. Stewart. 2000. Working strokes by single molecules of the kinesin-related microtubule motor ncd. Nat. Cell Biol. 2:724–729.

[24] Howard, J. 2001. Mechanics of motor proteins and the cytoskeleton. Sunderland, MA: Sinauer.

[25] Endow, S. A., and H. Higuchi. 2000. A mutant of the motor protein kinesin that moves in both directions on microtubules. Nature. 406:913–916.

[26] Badoual, M., F. Julicher, and J. Prost. 2002. Bidirectional cooperative motion of molecular motors. Proc. Natl. Acad. Sci. USA. 99:6696–6702.

[27] Lowe, J., H. Li, K. Downing, and E. Nogales. 2001. Refined structure of $\alpha beta$-tubulin at 3.5 Å resolution. J. Mol. Biol. 313:1045–1057.

[28] Sindelar, C. V., and K. H. Downing. 2007. The beginning of kinesin's force-generating cycle visualized at 9 Å resolution. J. Cell Biol. 177:377.

[29] Sindelar, C. V., and K. H. Downing. 2010. An atomic-level mechanism for activation of the kinesin molecular motors. Proc. Natl. Acad. Sci. USA. 107:4111–4117.

[30] Rasmussen, R., D. Benvegnu, E. K. O'Shea, P. S. Kim, and T. Alber. 1991. X-ray scattering indicates that the leucine zipper is a coiled coil. Proc. Natl. Acad. Sci. USA. 88:561–567.

[31] Miki, H., Y. Okada, and N. Hirokawa. 2005. Analysis of the kinesin superfamily: insights into structure and function. Trends Cell Biol. 15:467–476.

[32] Endow, S. A., and K. W. Waligora. 1998. Determinants of kinesin motor polarity. Science. 281:1200–1202.

[33] Song, H., M. Golovkin, A. Reddy, and S. A. Endow. 1997. *In vitro* motility of AtKCBP, a calmodulin-binding kinesin protein of *Arabidopsis*. Proc. Natl. Acad. Sci. USA. 94:322.

[34] Kuriyama, R., M. Kofron, R. Essner, T. Kato, S. Dragas-Granoic, C. K. Omoto, and A. Khodjakov. 1995. Characterization of a minus end-directed kinesin-like motor protein from cultured mammalian cells. J. Cell Biol. 129:1049–1059.

[35] Furuta, K. M., Y. Maeda, and Y. Toyoshima. 2008. Diffusion and directed movement: In vitro motile properties of fission yeast kinesin-14 Pkl1. J. Biol. Chem. 283:36465–36473.

[36] Endow, S. A., S. J. Kang, L. Satterwhite, M. Rose, V. Skeen, and E. Salmon. 1994. Yeast kar3 is a minus-end microtubule motor protein that destabilizes microtubules preferentially at the minus ends. EMBO J. 13:2708–2713.

Supporting Movies

Movie S1. RP-TMD of the Ncd dimer. The unbound motor head (dark blue) travels passively with the neck. A tubulin dimer (PDB 1JFF, purple and orange; (27)) is shown as a reference. Orientation of the motor head on the tubulin dimer is based on PDB 2P4N (28).

Movie S2. Two-step forward RP-TMD. After the initial motor head rearrangement, the neck moves in substeps defined in Figs. 2 and 5B. Ncd is colored as in Fig. 1.

Movie S3. Hysteresis in the neck motion. In the forward travel, the R335-D424 bond breaks at substep **2** while in the reverse travel, it forms only when the neck returns close to the pre-stroke position (substep **1**). Coloring scheme is similar to Fig. 5C.

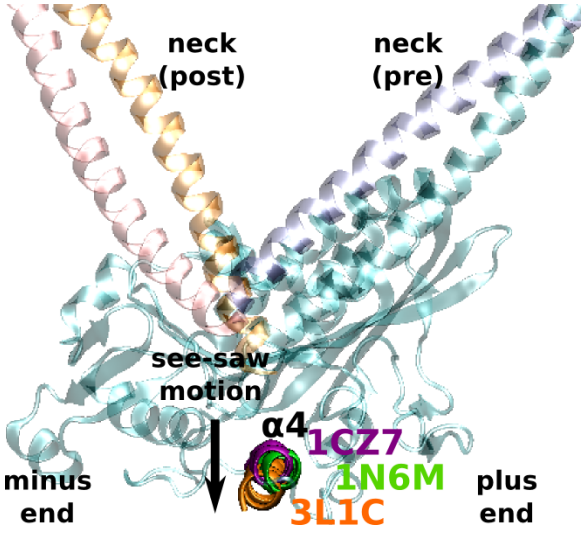

Figure S1: Conformation of $\alpha 4$ in different crystal structures. Viewing direction is the same as in Fig. 1. In PDB 3L1C, $\alpha 4$ is further away from the MH (the see-saw motion) (29), and the C-terminal tail points to a direction similar to the docked neck linker in Kinesin-1. Both PDB 1N6M and 3L1C have the neck in the post-stroke orientations despite the difference in the conformation of $\alpha 4$. Using either of them as a post-stroke conformation in RP-TMD does not affect the result significantly (Fig. 3C,G).

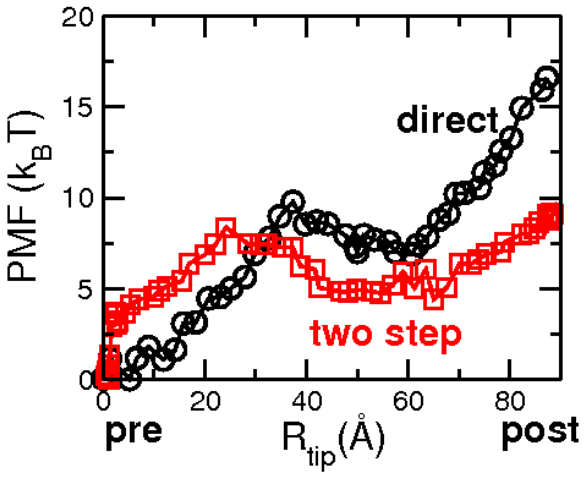

Figure S2: Comparison between the PMFs of the one-step RP-TMD (the neck travels before the MH rearrangement) and the two-step RP-TMD (neck travels after the MH rearrangement). The PMF for the latter case is from Fig. 5B. For the PMF calculation, we used RP-TMD trajectories with the same simulation conditions (ACE2 implicit solvent and MAXF=0.1; Table S1).

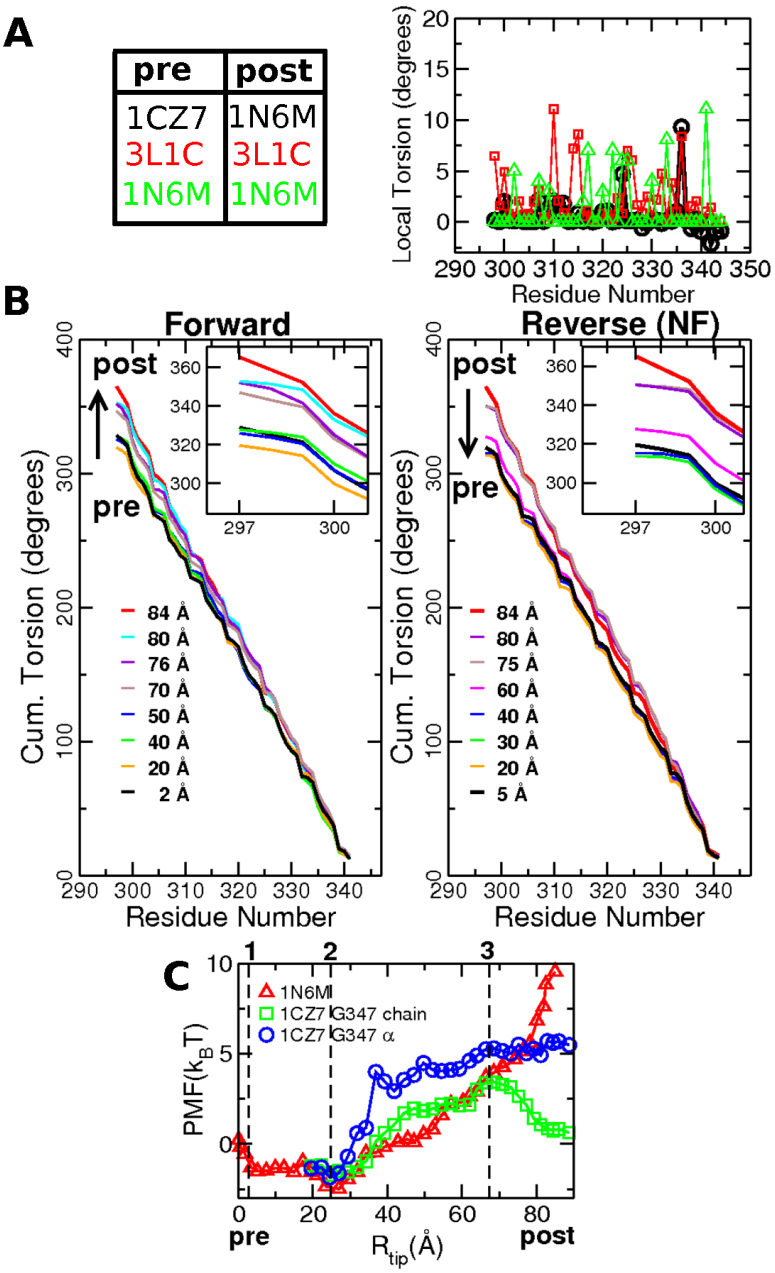

Figure S3: Torsional deformation of the Ncd neck and its contribution to the PMF. (A) Distribution of torsional strains on the neck coiled-coil with different pre- and post-stroke structures used. Vertical axis is the local twist angle of the neck in the post-stroke relative to the pre-stroke structure. Overall positive angles suggest unwinding of the left-handed coiled-coil. (B) Cumulative torsional angle at different values of $R_{\rm tip}$ for the trajectory in Figs. 2 and 5. Torsion develops mostly in the region $R_{\rm tip} > 60$ Å. (C) Contribution of the torsion of the neck to the PMF. Red triangle: PMF for the WT (Fig. 5B, rev NF). Green square: Neck in the pre-stroke conformation of PDB 1CZ7 (lacking torsional strain) used for the post-stroke conformation, including G347 in the random-coil state (*cf.*, Fig. 4C). Blue circle: With the 1CZ7 neck, but G347 in the post-stroke α-helical conformation. The sharp change in PMF between **3** and the post-stroke state is absent in the chimeras. The PMF curves for the chimeras were vertically shifted to match with the WT PMF at $R_{\rm tip} = 19.5$ Å.

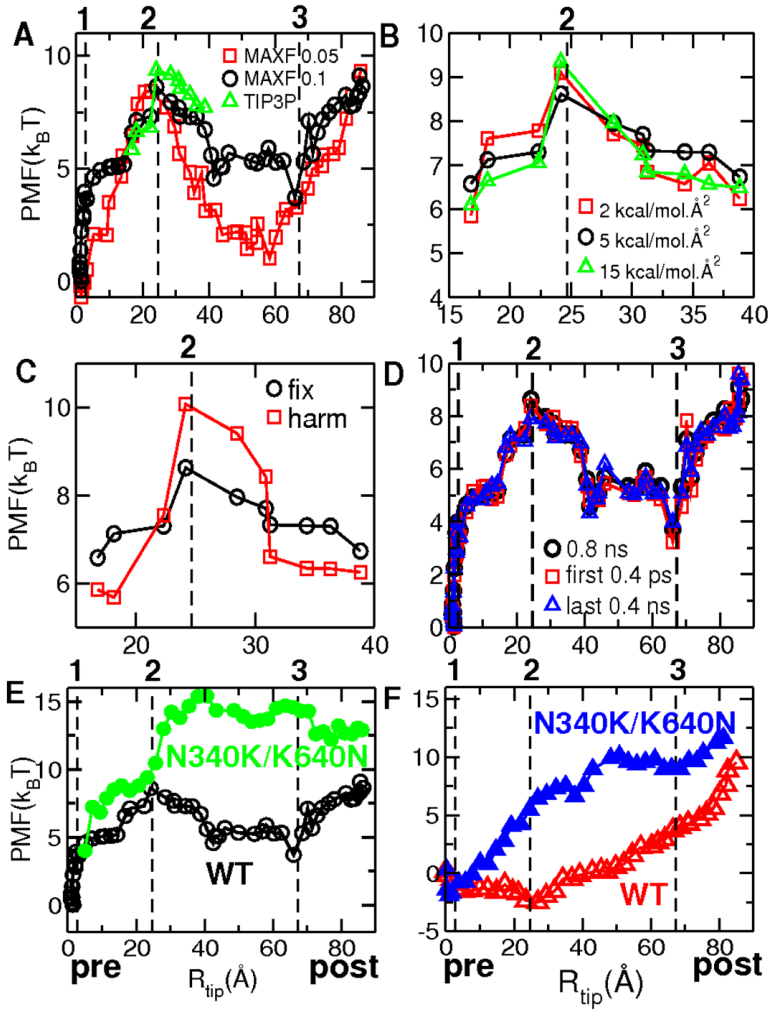

Figure S4: Testing the reliability of the calculated PMF for WT (A–D), and PMF of the double mutant N340K/K640N (E,F). (A) Comparison between PMF curves calculated using different TMD trajectories in the ACE2 implicit solvent (MAXF=0.1 and 0.05), and in explicit water. For the explicit-water trajectory, TOWS was carried out using the GBSW implicit solvent model, which is known to match the analytic Poisson-Boltzmann result within 2% error (19). (B) PMF curves around the barrier **2** obtained using different spring constants in TOWS. (C) Using harmonic constraints on the MH backbone instead of fixing the domains of the MH that do not interact with the neck. Although changes in energy is somewhat different, the overall profile including the location of the peak is the same. (D) Dividing the 0.8-ns sampling interval into two and calculating PMF for each, which resulted in very little change. For the TIP3P simulation in (A), and the simulations in (B) and (C), the sampling was performed only around the neighborhood of **2**, and the corresponding PMFs were vertically shifted to compare with the reference PMF. (E) Forward and (F) reverse PMFs of the double mutant N340K/K640N.

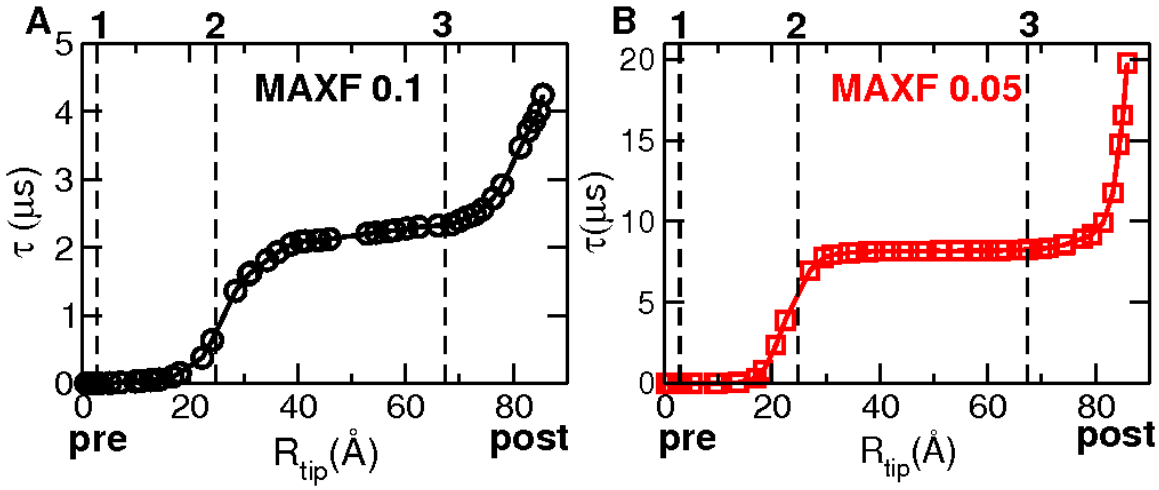

Figure S5: First passage time for the Ncd's neck to reach R_{tip} from the pre-stroke position. (A) MAXF= 0.1, (B) MAXF= 0.05. The PMFs used are from Figs. 5B and S4A.

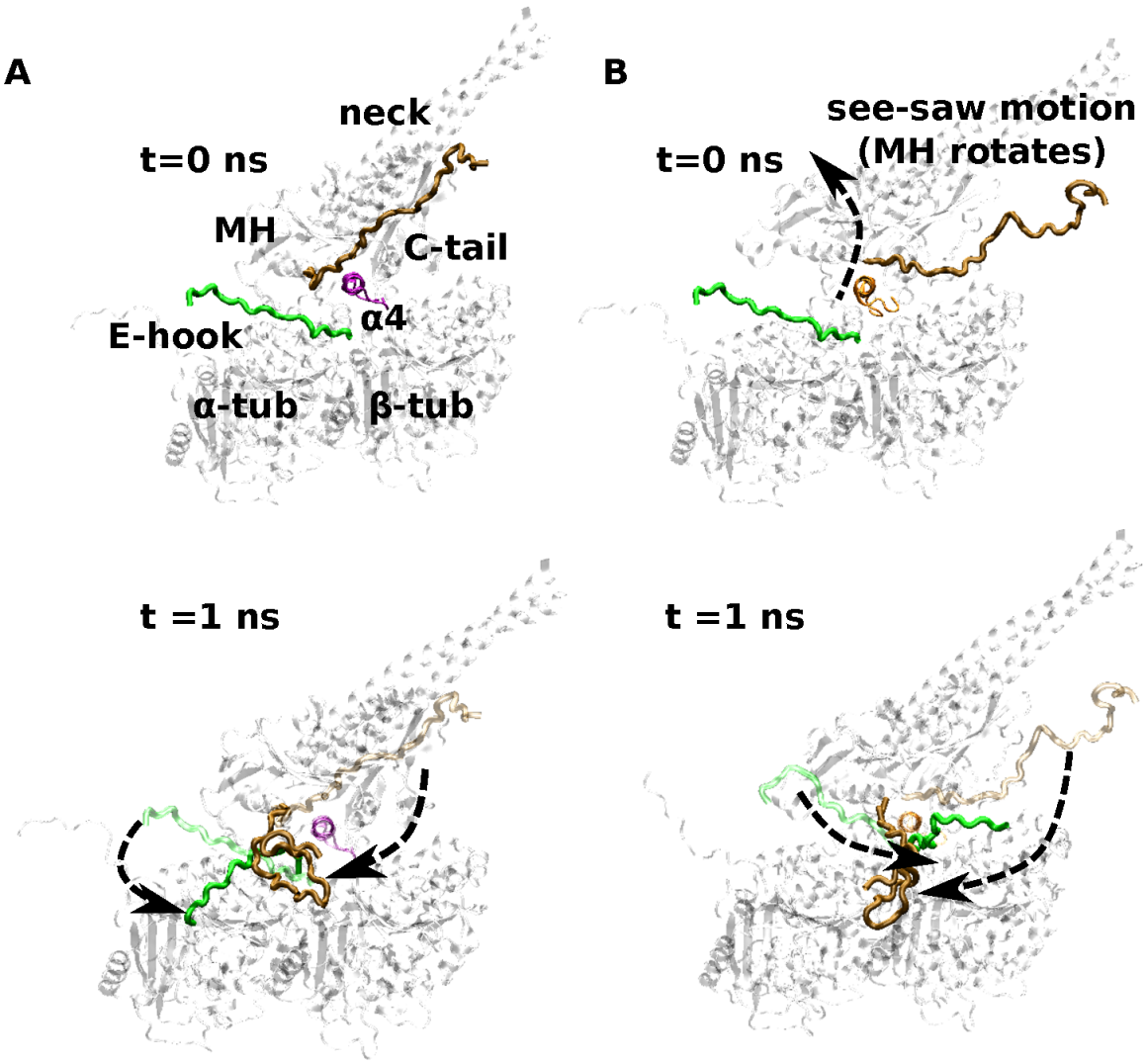

Figure S6: A model of MT-bound Ncd with the C-tail and the MT E-hooks. The MH is in (A) ADP state (PDB 1CZ7) and (B) ATP-like state (PDB 3L1C) (Fig. S1). The coloring scheme of $\alpha 4$ is the same as in Fig. S1. Orientation of the MH on the tubulin dimer (PDB 1JFF) (27) is based on PDB 2P4N (28), as in Movie S1. All-atom explicit water simulations were performed using GROMACS (333,455 atoms in total) to relax the structure. At $t = 0$ ns (top row), (A) due to the blocking orientation of $\alpha 4$ (purple), the C-tail comes out of the MH in a direction perpendicular to the page, whereas in (B) it points to the MT plus-end, since $\alpha 4$ (orange) is out of the way (dashed arrow; Fig. S1). After 1 ns (bottom row), the C-tail and the E-hook of β-tubulin move and make contact in both cases (dashed arrows). In (B), since $\alpha 4$ is stationary on the MT, the see-saw motion (Fig. S1) causes the MH to rotate clockwise when viewed from the MT plus-end.

Motor	Direction of Motion	MAXF (Å)	Pre (PDB)	Post (PDB)	Solvent model	Time (t) (ps)	No. of Runs
WT	Forward (pre→post)	0.05	1CZ7	1N6M	ACE2	87.3±5.2	10
					FACTS	79.4±10.2	
		0.1	1CZ7	1N6M	ACE2	53.3±7.1	
					FACTS	45.2 ± 12.4	
					TIP3P	207	1
		0.1	1N6M	1N6M	ACE2	41.8 ± 9.7	10
					FACTS	30.4± 12.4	
			3L1C	3L1C	ACE2	49.8 ± 6.9	
	Reverse (post→pre)	0.05 (NF)	1CZ7	1N6M	ACE2	52.7 ± 7.2	10
		0.1(HF)	1CZ7	1N6M	ACE2	57.8 ± 11.3	
		0.1(NF)	1CZ7	1N6M	ACE2	47.3 ± 15.2	
					FACTS	42.4 ± 12.4	
					TIP3P	143	1
			1N6M	1N6M	ACE2	62.7 ± 8.2	10
			3L1C	3L1C	ACE2	54.5 ± 23.1	
R335A	Forward (pre→post)	0.1	1CZ7	1N6M	ACE2	37.2 ± 5.7	10
N340A						38.7 ± 3.5	
N340K						47.2 ± 12.6	
D344A						56.2 ± 11.4	
K640A						47.2 ± 9.2	
K640N						62.5 ± 7.6	
R335A/K336A						44.2 ± 7.1	
N340K/K640N						55.3 ± 20.3	
Ncd-ran12						29.8	1
LZ-neck						20.2	1
D344A	Reverse (post→pre)	0.1(NF)	1CZ7	1N6M	ACE2	47.1 ± 11.2	10
N340K/K640N						42.8 ± 9.1	
Ncd-ran12						34.1	1

Table S1: Conditions used in RP-TMD simulations. The pre- and post-stroke conformations of 1N6M or 3L1C are respectively from chain A and B in the PDB file. The simulation stopped at time t when the root-mean-square deviation of the system from the target structure fell below 0.8 Å. 'HF' and 'NF' refer to two different ways for the reverse motion mentioned in Fig. 5. Mutations are from Refs. 7, 25. Ncd-ran12 is a 12 residue substitution where the 335RKELHNTVMDLR346 in the WT neck was replaced by 335ESGAKQGEKGES346 (7). For the LZ-neck, the Ncd neck residues 320ELETCKEQLFQSNMERKEL-HNTVMDLR346 were replaced with that of a leucine zipper sequence 320KLMKQLEDKVEELLSKNYH-LENEVARLK346 (30). MAXF: Maximum allowed perturbation in RP-TMD (6).

	Neck	MH					v_m(μm/min)
	α_0	β_1	α_1	α_2	$L10$	$L13$	
Ncd	325**K E Q** - - - L **F** Q S N **M** E - - - - - - - - - - **R K** E - L **H N** T V **M D** 344	349I **R** 350	413**E** **M** V S **P L** I **Q S** A L **D** G **Y** 426	470**N L** G **W** 473	567**E K** 568	639S **K** 640	**8.4–15.2**
Kcbp	805 *Y K* **Q** - - - - - - EQ V L - - - - - - - - - - **R K** R - Y *Y* N T I E **D** 820	815I **R** 816	884**E** D TK Y L V **Q S** A V **D** G **Y** 897	941**N** - K Y 943	1038 *Q T* 1039	1113A **K** 1114	**8–12**
Cho2	234 *A* **E Q** G D R L H G L E M E - - - - - - - - - - **R R** R - L **H N** Q L Q **E** 256	261I **R** 262	336**E** E I S M L V **Q S** A L **D** G **Y** 352	396 *G* Q G W 399	501 *A* **R** 502	581A **K** 582	**1.0–8.4**
Pkl1	446 *Q Q L* - - - E R R N E D M Y N K L L A E E I I R **R R** K - L **H N** D I Q **E** 475	480I **R** 481	554**E** E I S Q L I **Q S** A I **D** G **Y** 567	608 *E* K G W 611	708 *R T* 709	791A **K** 792	**2.76**
Kar3	363 *N* **E** *I* - - - L I K E E T V - - - - - - - - - - **R R** T - L **H N** E L Q **E** 382	387I **R** 388	453 *K* E V G Q L V **Q S** S L **D** G **Y** 466	508 *T* K G W 511	613 *K T* 614	692S **K** 693	**1–2**
Kifc1	289 *G* **D** *R* - - - L Y G L E M E - - - - - - - - - - **R R** R - L **H N** Q L Q **E** 307	312I **R** 313	390**E** E I A M L V **Q S** A L **D** G **Y** 403	451 *G* Q G W 454	553 *A* **R** 554	633A **K** 634	
Kifc2	385**K** *T* **Q** - - - L S E G N Q A - - - - - - - - - - *P P* T G C *S G* R L L **E** 404	409I **R** 410	465 *R* Q L E P A V *L* **S** C L *Q* G **Y** 478	518 *G* T G G 521	616 *P* **R** 617	701T *T* 702	
Kifc3	411 *I* **E** *E* - - - V N S N N Q E L L R K Y R R E L Q L **R K** K - C **H N** E L V *R* 439	444I **R** 445	505 *Q* E V Q A L I *T* **S** C I **D** G *F* 518	561 *A* S D W 564	659 *S T* 660	701T *T* 702	
Kin1	701 *V* **E Q** - - - Q I Q S H - - - - - - - - - - - - **R** *E* T - H *Q K* Q I S *S* 718	9I **K** 10	64**D** C A K K I V *K D* V L **E** G **Y** 78	123 *D* E N L 126	218 *Q T* 219	294C **R** 295	**42**

Table S2: Comparison of the amino acid sequence and MT gliding velocities in the Kinesin-14 family. Kinesin names are from (31). Residues corresponding to those forming the MH-neck contacts in Ncd are highlighted in boldface, and colored blue and red. On these sites, residues that deviate from those of Ncd are shown in italic. In Kar3, K453 replaces E413 of Ncd that forms the K336-E413 bond (Fig. 1), which may be related to its slower MT gliding velocity. Residues of Ncd forming hydrophobic contacts between the MH and the neck are colored in green. They show poorer conservation except for L418, which faces the central β-sheet of the MH core (Fig. 4A). Sequence comparison with Kinesin-1 (Kin-1) shows critical differences in the sites where the neck interacts. Note that Ncd's neck matches with a C-terminal region of the stalk of Kinesin-1. Gliding velocities are from: Ncd (7, 32), Kcbp (33), Cho2 (34), Pkl1 (35), Kar3 (36), and Kin1 (7).